





ARTICLE

DOI: 10.1038/s41467-018-06776-z

OPEN

Narrow bandgap oxide nanoparticles coupled with graphene for high performance mid-infrared photodetection

Xuechao Yu ¹, Yangyang Li², Xiaonan Hu¹, Daliang Zhang ³, Ye Tao¹, Zhixiong Liu², Yongmin He¹, Md. Azimul Haque², Zheng Liu ⁴, Tom Wu^{2,5} & Qi Jie Wang ¹

The pursuit of optoelectronic devices operating in the mid-infrared regime is driven by both fundamental interests and envisioned applications ranging from imaging, sensing to communications. Despite continued achievements in traditional semiconductors, notorious obstacles such as the complicated growth processes and cryogenic operation preclude the usage of infrared detectors. As an alternative path towards high-performance photodetectors, hybrid semiconductor/graphene structures have been intensively explored. However, the operation bandwidth of such photodetectors has been limited to visible and near-infrared regimes. Here we demonstrate a mid-infrared hybrid photodetector enabled by coupling graphene with a narrow bandgap semiconductor, Ti_2O_3 ($E_g = 0.09$ eV), which achieves a high responsivity of 300 A W^{-1} in a broadband wavelength range up to $10 \mu\text{m}$. The obtained responsivity is about two orders of magnitude higher than that of the commercial mid-infrared photodetectors. Our work opens a route towards achieving high-performance optoelectronics operating in the mid-infrared regime.

¹Centre for OptoElectronics and Biophotonics, School of Electrical and Electronic Engineering & The Photonics Institute, Nanyang Technological University, 639798 Singapore, Singapore. ²Materials Science and Engineering, King Abdullah University of Science and Technology, Thuwal 23955-6900, Saudi Arabia. ³Imaging and Characterization Core Lab, King Abdullah University of Science and Technology, Thuwal 23955-6900, Saudi Arabia. ⁴Centre of Programmable Materials, School of Materials Science and Engineering, Nanyang Technological University, 50 Nanyang Avenue, 637371 Singapore, Singapore. ⁵School of Materials Science and Engineering, University of New South Wales (UNSW), Sydney, NSW 2052, Australia. Correspondence and requests for materials should be addressed to T.W. (email: tom.wu@unsw.edu.au) or to Q.J.W. (email: qjwang@ntu.edu.sg)

High-performance infrared photodetectors that can convert light into electrical signals lead to a wide range of applications ranging from imaging sensors to optical communications^{1–3}. Practically, long-wavelength infrared (LWIR) detectors are expected to have features of high photon-carrier conversion efficiency, low noise level at room temperature and fast response speed in a broadband wavelength range. It still remains as a challenge to realize high performance LWIR photodetection with the conventional narrow-bandgap semiconductors such as mercury cadmium telluride (HgCdTe) thin films, indium antimonide (InSb) and artificial semiconductor superlattices via inter/intraband transitions⁴. Recently, significant efforts have been devoted to colloidal quantum dots (CQDs) based photodetectors due to their high absorption efficiency and facile manufacturing processes⁵. However, CQDs-based photodetectors suffer from limited operation spectral bandwidth because of their relatively large bandgaps^{6,7}. Alternatively, two-dimensional materials appear to be promising candidates and provide unique properties such as ultrahigh carrier mobility, easy-integrability and broadband light absorption⁸. Graphene has been successfully demonstrated as a broadband photodetector from visible to the terahertz wavelength regimes^{9–14}. Unfortunately, the intrinsic low absorption and fast carrier recombination rate of graphene hinder its application in photodetection, and such devices suffer from low responsivity as well as poor detectivity¹⁵.

Several pioneering works have been devoted to improving the performance of graphene-based photodetectors through constructing hybrid structures. Ultrahigh optical gain was achieved in hybrid graphene-CQD structures, where graphene serves as the ultrahigh speed carrier transport channel and CQD serves as light absorber with high absorption efficiency^{16,17}. In such hybrid structures, one type of carrier (either electron or hole) is trapped in the CQD while the other type rapidly circulates in the graphene channel driven by the external source-drain voltage. Similar designs were also employed in the photodetectors with hybrid graphene-TiO₂¹⁸, graphene-ZnO¹⁹, graphene-dye²⁰, and graphene-perovskite structures²¹. However, the operation wavelength of such hybrid photodetectors are limited in the visible and the near-infrared regimes owing to the relatively large intrinsic bandgap of the light absorbers⁹. Although black phosphorene^{22–25} and noble metal dichalcogenides have been recently demonstrated as a near-infrared/mid-infrared semiconductor²⁶, it still remains as a challenge to further improve the performance of photodetectors in terms of photon absorption efficiency, responsivity, and response speed in the important mid-infrared regime.

Here we demonstrate room-temperature mid-infrared photodetectors with high responsivity, detectivity and high speed, realized by hybridizing graphene with a novel narrow bandgap semiconductor, titanium sesquioxide (Ti₂O₃) nanoparticles. Ti₂O₃, a stable semiconductor with extraordinary broadband photoresponse characteristics, has a narrow-band gap of 0.09 eV, corresponding to a cut-off absorption wavelength of 13.3 μm²⁷. The working mechanism is as follows: when the incident light is absorbed by the Ti₂O₃ nanoparticles, the photo-excited electrons are trapped in the Ti₂O₃ nanoparticles, while the holes are transferred into the graphene channel, leading to a conspicuous photocurrent measured in a field effect transistor configuration. In addition, we also systematically investigated the photo-generated carrier transfer processes at the interface of graphene and Ti₂O₃ in this hybrid photodetector. The developed graphene/Ti₂O₃ photodetector is demonstrated to be capable of operating in both accessible atmospheric windows, the mid-wavelength infrared (MWIR: 3–5 μm) and the LWIR (8–12 μm) regimes. The broadband mid-infrared operation bandwidth, high responsivity and detectivity make the graphene/Ti₂O₃ a promising candidate

for mid-infrared photodetection, providing a novel paradigm for mid-infrared photonics and optoelectronics.

Results

Band structure and optical properties of Ti₂O₃. The schematic diagram of the proposed hybrid graphene/Ti₂O₃ photodetector is illustrated in Fig. 1a, representing the architecture of the graphene channel decorated with the narrow-bandgap Ti₂O₃ nanoparticles as indicated in Supplementary Method. Ti₂O₃ exhibits strong light absorption in the infrared regime with wavelength shorter than 13.3 μm, thus it can be used as an efficient light absorber in the MWIR and LWIR regimes. Once electron-hole pairs are mainly generated in the Ti₂O₃ nanoparticles with light illumination, the charge transfer process occurs at the graphene/Ti₂O₃ interface (Fig. 1b), leading to the conductance modulation of the graphene channel and thus the photodetection. The crystal structure of Ti₂O₃ is shown in Fig. 1c, which shows a corundum structure with a trigonal unit cell ($a = b = 5.15 \text{ \AA}$; $c = 13.61 \text{ \AA}$). Ti₂O₃ is chosen in this hybrid structure as the light absorber owing to its unique narrow bandgap (0.09 eV) that covers the mid-infrared regime²⁷. Ti₂O₃ is very different from the well-studied wide bandgap semiconductor TiO₂, as shown in Supplementary Figure 1. To understand the electronic structure and nature of the band edge wavefunction of Ti₂O₃, density functional theory (DFT) calculations with a plane-wave basis set were performed. The calculation details are given in the Supplementary Note 1. As shown in Fig. 1d, e, band realignments occur in the density of states (DOS) of Ti₂O₃ due to its unpaired 3d electrons, which contributes to the states just below the conduction band and forms an upper valence band, as shown in Fig. 1f. The narrow bandgap of Ti₂O₃ is located between the lower and the upper Hubbard band^{28–31}, which is estimated to be about 0.09 eV according to the absorption spectrum in Fig. 1g. In contrast, the bandgap of TiO₂ is about 3.3 eV and originated from the separation between O 2p and Ti 3d orbitals. The unique and wide-band light absorption of Ti₂O₃, as shown in Fig. 1f, especially in the mid-infrared range, makes it suitable for creating pertinent mid-infrared optoelectronic devices.

Ti₂O₃ nanoparticles with relatively uniform nanoparticle sizes were prepared by a simple ball milling process followed by ultrasound process and purification in ether solution. Then they were spin-coated on the channel surface of a graphene field effect transistor (FET). As shown in the X-ray diffraction (XRD) pattern in Fig. 2a, the Ti₂O₃ nanoparticles exhibit the corundum phase, which is consistent with the previous reports^{27,31}. As shown in Fig. 2b and the Supplementary Figure 2, the obtained Ti₂O₃ nanoparticles have an average diameter of ~50–200 nm, characterized by scanning electron microscopy (SEM). Furthermore, high-resolution transmission electron microscopy (HR-TEM) and selected-area electron diffraction (SAED) were performed to characterize the structure of the fabricated Ti₂O₃ nanoparticles. As shown in Fig. 2c, the lattice constants of ~0.37 nm and ~0.26 nm correspond to the (012) and (104) planes, respectively, in the corundum (trigonal) Ti₂O₃ lattice. Moreover, the corresponding SAED pattern shown in Fig. 2d demonstrates the high crystalline quality of the Ti₂O₃ nanoparticles. The Raman spectrum of the Ti₂O₃ nanoparticles shows seven active Raman modes (Fig. 2e), which is characteristic of corundum Ti₂O₃ (space group: R-3c). X-ray photoelectron spectroscopy (XPS) was used to characterize the electronic states of Ti and O in the Ti₂O₃ nanoparticles. As shown in Fig. 2f, the Ti 2p_{3/2} peaks with binding energies of 456.8 and 462.5 eV arise from spin-orbit splitting, corresponding to Ti³⁺ in Ti₂O₃³². In addition, the peak with a binding energy of 529.6 eV in the O 1s spectrum (Fig. 2g) is consistent with the electronic state of oxygen in Ti₂O₃³³.

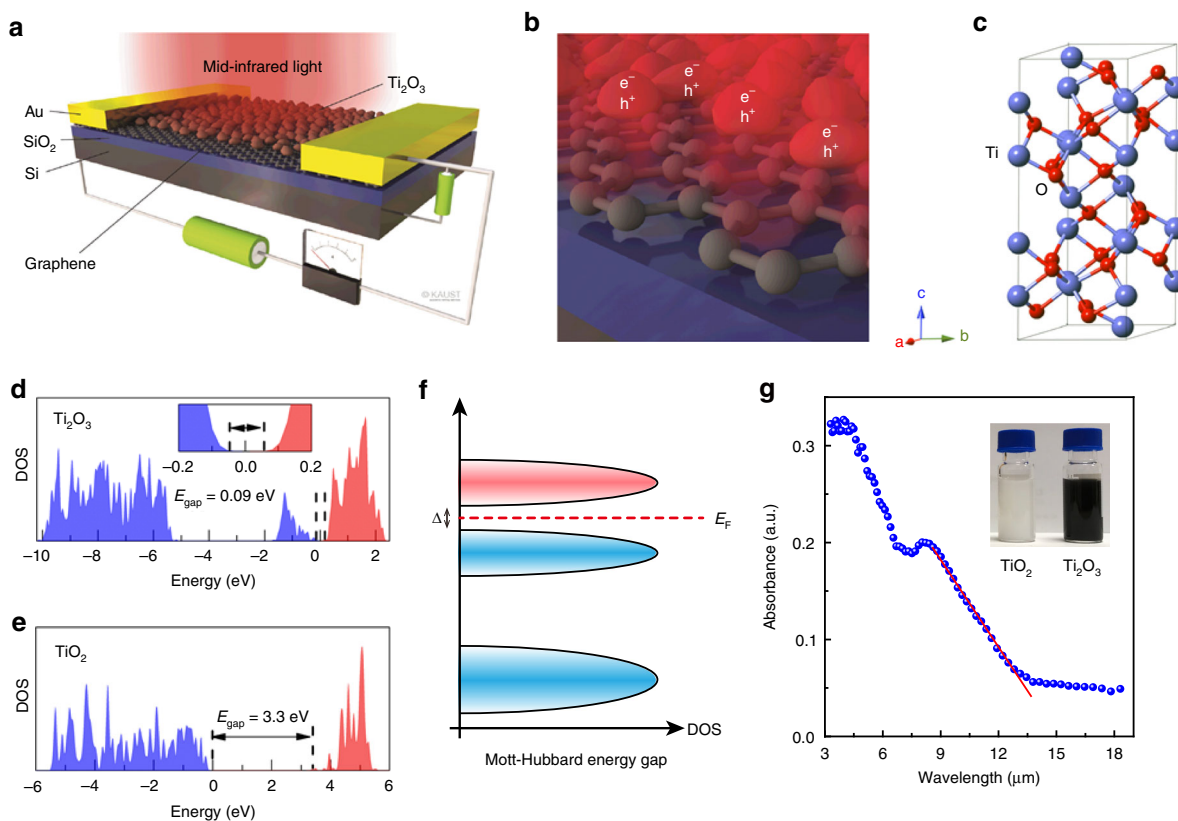


Fig. 1 Hybrid graphene/ Ti_2O_3 nanoparticle mid-infrared photodetector. **a** A schematic diagram of hybrid graphene/ Ti_2O_3 nanoparticle photodetector. **b** Illustration of the interface between Ti_2O_3 nanoparticles and graphene. **c** Crystal structure of corundum Ti_2O_3 . **d, e** Density of states (DOS) of Ti_2O_3 and TiO_2 derived from first principle calculations, respectively. Blue and red areas represent O 2p and Ti 3d orbitals, respectively. **f** Schematic band diagram of Ti_2O_3 , indicating that a narrow bandgap is formed between upper Hubbard band (pink) and lower Hubbard band (blue) as a result of strong electron correlation. **g** Absorption spectrum of Ti_2O_3 nanoparticles drop-casted on a KBr substrate, measured through Fourier Transform Infrared Spectroscopy. The cut-off wavelength is about $13.3\ \mu\text{m}$, which corresponds to a band gap of $0.09\ \text{eV}$. The inset is a photo of TiO_2 and in Ti_2O_3 nanoparticles in ether solution

Charge transfer processes in hybrid graphene/ Ti_2O_3 . To examine the interaction between graphene and Ti_2O_3 in the hybrid structure, Raman spectroscopy was applied to monitor the charge transfer between Ti_2O_3 and graphene under laser illumination. The positions of the characteristic Raman peaks such as the G peak and 2D peak of graphene are sensitive to the carrier density which can be modulated by doping and external electrical bias^{34,35}. Hereafter, if not especially declared, graphene refers to monolayer graphene. The doping effect in graphene caused by the charge transfer is investigated by examining the shifts of the G peak and 2D peak. As shown in Fig. 3a, b, both the G peak and the 2D peak exhibit weak redshift in the Raman spectra after the deposition of Ti_2O_3 on top of graphene channel. The redshift of G peak indicates the *p*-type doping effect induced by the charge transfer (holes) from Ti_2O_3 to graphene in the hybrid structure³⁴. Notably, as fabricated Ti_2O_3 is a *p*-type semiconductor³⁶, and our fabricated pristine graphene is also *p*-type due to the absorbed hydrocarbon molecules or humidity. As a result, the charge transfer in this hybrid structure remains inefficient because of the band misalignment between graphene and Ti_2O_3 , which contributes to the weak shift of the G peak shown in Fig. 3a.

We thus applied gate voltages to modulate the Fermi level of graphene and align the band structure between graphene and Ti_2O_3 to investigate the charge transfer process in the hybrid structure. Figure 3c, d display the gate-dependence of the G peak and 2D peak positions. Clearly, both G peak and 2D peak show clear redshift when the gate voltage changes from -80 to $80\ \text{V}$, which are more significant than the unbiased cases (as shown in

Fig. 3a, b). The shift of these Raman peaks provides paramount insights into the charge transfer at the graphene/ Ti_2O_3 interface^{37–39}. The 2D peak is derived from a second-order, double-resonant Raman scattering mechanism and its frequency decreases with increasing gate voltage that up-shifts the Fermi level of graphene³⁴. Theoretically, it is proven that with the increase of gate voltage, the G peak which is originated from the coupling between G-phonon lattice vibrations and Dirac fermions should present first blue-shift in the *p*-type doping regime ($V_g < V_D$) for graphene and then red-shift in the *n*-type doping regime ($V_g > V_D$) for graphene³⁸. This is contrary to the experimentally observed trend of G peak shown in Fig. 3c. We attribute the evolution of the G peak to the following two coexisting effects: the gating effect from the external bias and the charge transfer effect at the graphene/ Ti_2O_3 interface. In the *p*-type doped regime of graphene ($V_g < V_D$), the gating effect on graphene is the dominant contribution to the red-shifts of both G peak and 2D peak as the charge transfer process is suppressed, as shown in Fig. 3e. However, the hole transfer from Ti_2O_3 to graphene channel begins to dominate in the *n*-type doped regime of graphene ($V_g > V_D$) when the Fermi level is upshifted.

Mid-infrared photodetection under photoconductivity regime.

With the strong optical absorption of the Ti_2O_3 nanoparticles in the mid-infrared regime and the efficient charge transfer in the hybrid graphene/ Ti_2O_3 structure modulated by proper gate voltage, the mid-infrared photodetection performance of such hybrid photodetectors was demonstrated. The fabrication details

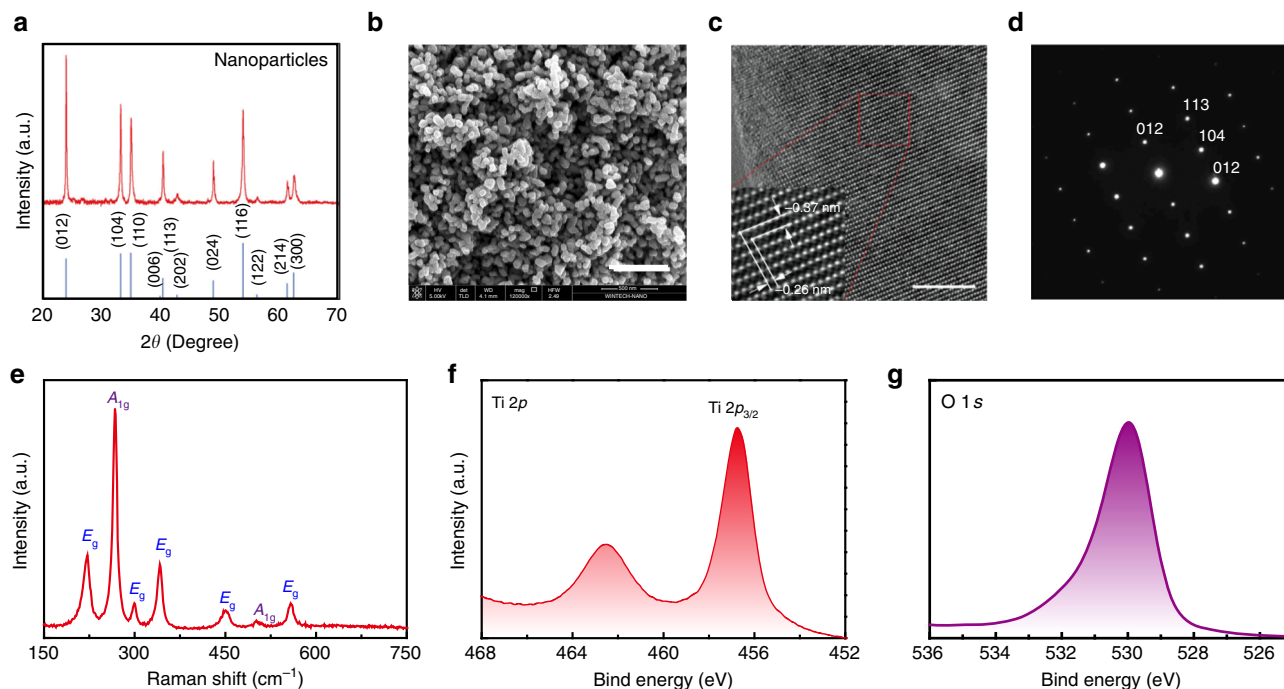


Fig. 2 Characterizations of the Ti_2O_3 nanoparticles. **a** X-ray diffraction (XRD) pattern of the Ti_2O_3 nanoparticles (red) together with the simulated XRD pattern from bulk corundum Ti_2O_3 (blue). **b** Scanning electron microscope (SEM) image of the Ti_2O_3 nanoparticles. Scale bar: 500 nm. **c** High resolution transmission electron microscope (HR-TEM) image of the Ti_2O_3 nanoparticles. Scale bar: 5 nm. Inset shows the enlarged lattice. **d** Corresponding selected area diffraction (SAED) pattern of the Ti_2O_3 nanoparticles. **e** Raman spectrum of the Ti_2O_3 nanoparticles. The seven characteristic peaks are indicated as $2A_{1g}+5E_g$. **f, g** X-ray photoelectron spectroscopy (XPS) of the Ti_2O_3 nanoparticles, depicting the Ti 2p and O 1s peaks, respectively

of the photodetector can be found in the Supplementary Method. Photodetection measurements were performed first under illumination by two quantum cascade lasers (QCL) with tunable wavelengths from $4\ \mu\text{m}$ to $7\ \mu\text{m}$ and $9.6\ \mu\text{m}$ to $10.6\ \mu\text{m}$, respectively, as indicated in Supplementary Note 2. As shown in Fig. 4a, b, electrical characterization is recorded both in dark and under the $10\ \mu\text{m}$ laser illumination. The I_d-V_d curves are generally linear and symmetric for small source-drain voltages, indicating ohmic-like electrode contacts. An obvious decrease of channel current is observed with laser irradiation, which is contributed by the photocurrent as shown in Fig. 4c. The gate-dependent photocurrent of the hybrid graphene/ Ti_2O_3 structure, which is defined as the absolute value of the source-drain current under the laser illumination subtracted by the dark current, is shown in Fig. 4b. The net photocurrent is almost negligible for gate voltage lower than the Dirac voltage (note that the pristine graphene as fabricated in our experiments is *p*-doped), which is consistent with the inefficient charge transfer due to the band misalignment between graphene and Ti_2O_3 in the hybrid structure, as shown in Fig. 3e. In contrast, the photocurrent increases when the gate voltage is higher than the Dirac voltage, indicating that the photogenerated holes are efficiently injected from Ti_2O_3 into graphene.

The hybrid graphene/ Ti_2O_3 photodetector shows a broadband photoresponse in the mid-infrared regime as shown in Fig. 4d and Supplementary Figure 5. As a demonstration example, a net photocurrent of $\sim 50\ \mu\text{A}$, corresponding to a responsivity of $\sim 120\ \text{A W}^{-1}$ under a source-drain bias of 2 mV, was achieved with $10\ \mu\text{m}$ laser illumination. This indicates that our hybrid photodetector offers low electrical power consumption. The obtained responsivity here vastly surpasses those in the previous reports on graphene- and other 2D-based mid-infrared photodetectors^{40–43}, which is about two orders of magnitude higher than that of

commercial mid-infrared photodetectors based on MCT, InSb and so on^{44–46}. Figure 4e exhibits the photoresponse measured in one on/off period with the subtraction of the dark current background. In addition, the response time is determined by the rising (falling) time from 10–90% (90–10%) of the photocurrent in Fig. 4e and Supplementary Figure 8. The rising and falling time was estimated to be $\sim 1.2\ \text{ms}$ and $\sim 2.6\ \text{ms}$, respectively. In the demonstrated photodetector, the response speed is limited by the scattering/trapping centers at the graphene/ Ti_2O_3 interface introduced during the device fabrication process⁴⁷. The device also demonstrated good stability during the on/off measurements, and the performance remains stable after several weeks if the device is properly kept. Furthermore, the hybrid graphene/ Ti_2O_3 photodetector shows versatile photoresponse in a broad spectrum range from $4.5\ \mu\text{m}$ to $10\ \mu\text{m}$ as shown in Fig. 4d and the Supplementary Figure 5, which is limited by the tuning range of our laser sources.

Discussion

The photoresponse of the hybrid graphene/ Ti_2O_3 photodetector presents a noteworthy enhancement when the graphene channel increases from monolayer to trilayer as shown in Fig. 4e. The electrical properties of the graphene FETs are indicated in Supplementary Figures 6–8. The layer-dependent charge transfer efficiency accounts for the competition between screening and absorption of the electric field of the dipoles of semiconducting Ti_2O_3 nanoparticles and the graphene layer as explained in Supplementary Figure 9 and Supplementary Note 3. We achieve an optimized responsivity of $\sim 300\ \text{A W}^{-1}$ for hybrid trilayer graphene/ Ti_2O_3 photodetector under $10\ \mu\text{m}$ laser illumination. Another prominent feature of the hybrid photodetector is its high detectivity as obtained from the low noise spectrum as shown in Fig. 4f. The spectral noise in the dark characterized by the setup

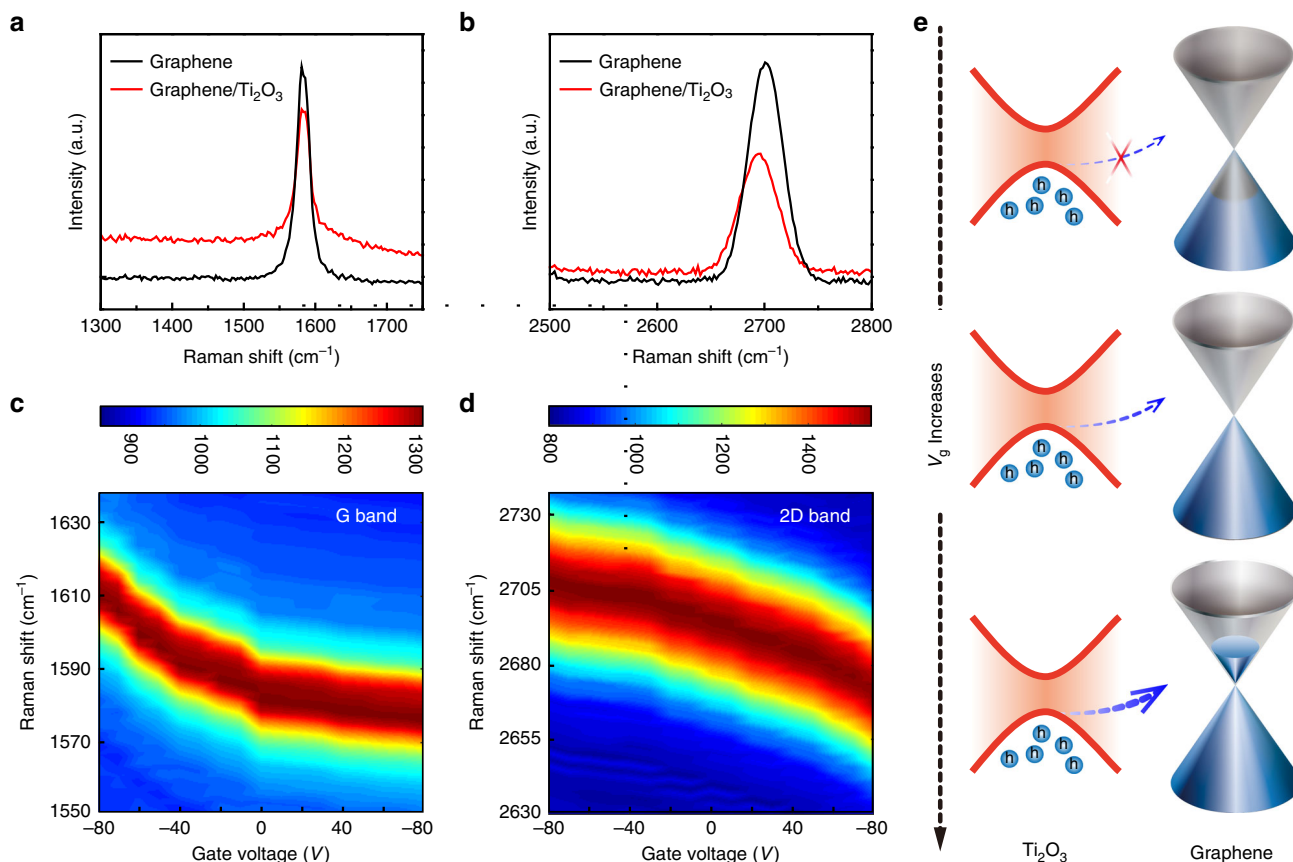


Fig. 3 Charge transfer and band alignment in the hybrid graphene/ Ti_2O_3 structure. **a** G-peaks ($\sim 1580\text{ cm}^{-1}$) of the Raman spectra measured on the hybrid graphene/ Ti_2O_3 and the reference graphene samples without gating voltage. **b** 2D-peaks ($\sim 2700\text{ cm}^{-1}$) of the Raman spectra measured on the same samples without gating voltage. **c, d** Evolution of the G and 2D Raman peaks, respectively, of the hybrid graphene/ Ti_2O_3 sample under different gate voltages. **e** Illustration of the band alignment and the charge transfer at the hybrid graphene/ Ti_2O_3 interface. It is illustrated that holes can only transfer from p-type Ti_2O_3 to the graphene layer when the graphene is gated properly. Gray and lightblue regimes represent conduction and valance band, respectively

as shown in Supplementary Figure 4 exhibits a concrete 1/f component, which is consistent with the previous reports for graphene-based FETs⁴⁸. The detectives, D^* , are calculated to be $\sim 2 \times 10^8\text{ cm Hz}^{1/2}\text{ W}^{-1}$, $3 \times 10^8\text{ cm Hz}^{1/2}\text{ W}^{-1}$, and $7 \times 10^8\text{ cm Hz}^{1/2}\text{ W}^{-1}$ for monolayer, bilayer and trilayer graphene according to Supplementary Equation 1, respectively, which are comparable with the current room-temperature operated MCT and bolometers^{43–45}. Graphene layer dependent photoresponse properties are shown in Supplementary Note 3. This concrete phenomenon additionally demonstrates the surface-mediated charge transfer effect of the abnormal behavior of this hybrid structure⁴⁶. The results here provide hints towards optimizing the 0D-2D hybrid infrared optoelectronic devices.

We further explored the effect of the size of Ti_2O_3 nanoparticles on the optoelectronic properties of the hybrid graphene/ Ti_2O_3 structure. As shown in Fig. 4g, the photocurrent increases with the decrease of the average size of Ti_2O_3 nanoparticles from 200 to 80 nm (the size is characterized by TEM as shown in Supplementary Figure 3); however, the photocurrent almost vanishes when the size drops to 50 nm as shown in Supplementary Figure 10. The effect on the size-dependent photocurrent can be attributed to the trade-off between charge transfer efficiency and light absorption efficiency, as explained in Supplementary Note 4. On the other hand, Ti_2O_3 thin films deposited on graphene layer by PLD method are characterized by Raman spectrum (Supplementary Figure 11) and patterned into FET channel

as shown in Supplementary Figure 12. The photoresponses of the Ti_2O_3 thin films based photodetector is also indicated in Supplementary Figure 13 and Supplementary Note 5. The exotic properties of the hybrid graphene/ Ti_2O_3 make it a promising candidate for mid-infrared photodetection. Moreover, as shown in Fig. 4h, compared with previous reports on similar hybrid photodetectors, the performance of our hybrid graphene/ Ti_2O_3 photodetector is superior to other systems such as pure graphene^{11–14}, black phosphorene^{22–25} and other similar semiconductor hybrid structures. By coupling graphene with narrow-bandgap Ti_2O_3 , such a hybrid photodetector has the advantages of operating at LWIR with high responsivity and speed. Possible strategy to improve the performance of such hybrid graphene/ Ti_2O_3 photodetectors is to further enhance the charge transfer rate and efficiency by engineering the surface states of graphene and Ti_2O_3 nanoparticles with chemical treatments or by introducing suitable ligands on the surfaces of Ti_2O_3 nanoparticles.

To summarize, room-temperature-operated photodetectors with high photoresponse in the mid-infrared regime were demonstrated using the hybrid graphene/ Ti_2O_3 structures. This type of hybrid photodetector exhibits a high responsivity that surpasses other two-dimensional materials based photodetectors and commercial photodetectors in the long-wavelength infrared range. The unparalleled performance demonstrated in this work hinges upon the highly efficient broadband absorption of Ti_2O_3 nanoparticles, as well as the fast carrier transport in graphene

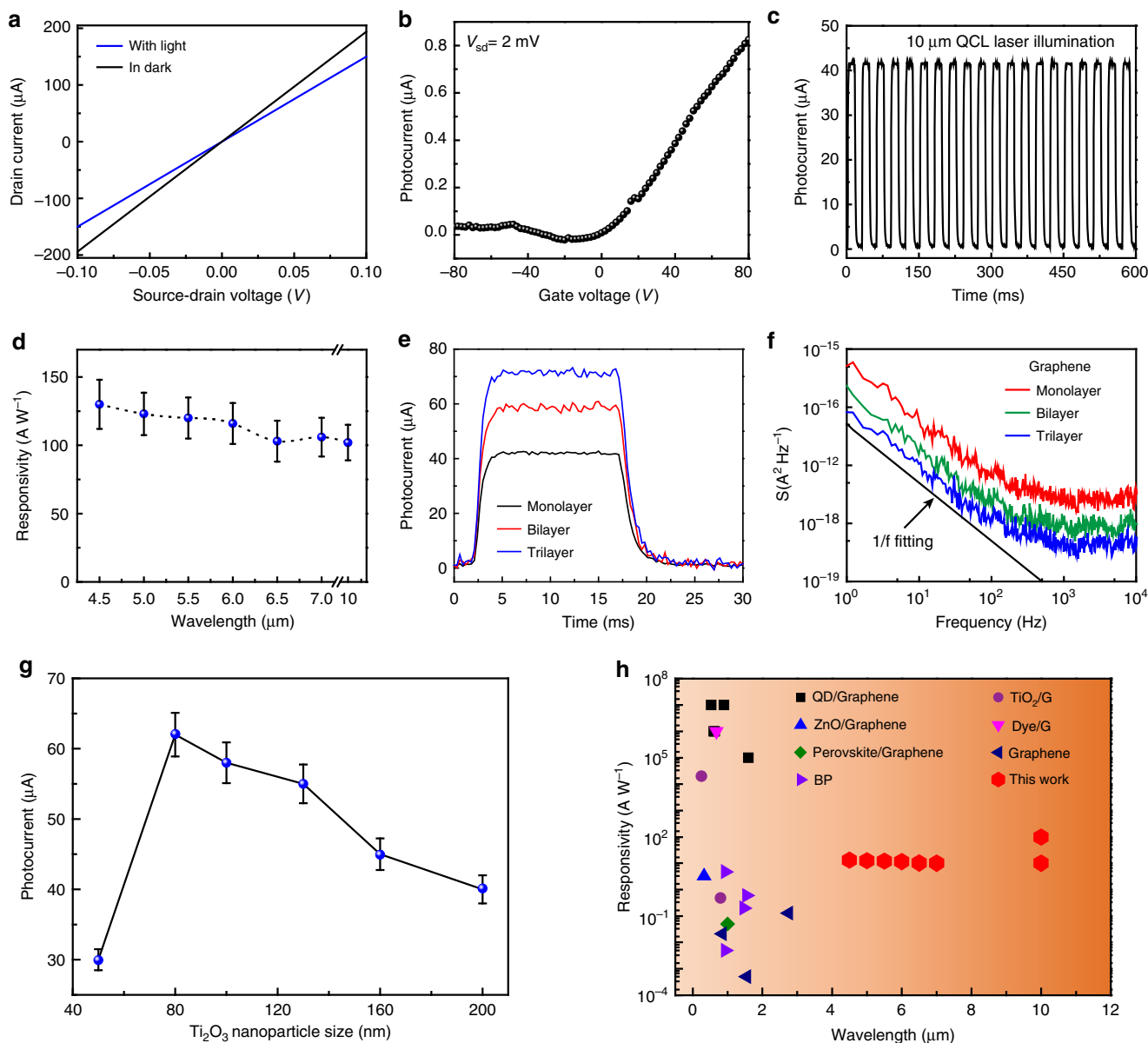


Fig. 4 Performance of the hybrid graphene/Ti₂O₃ photodetector. **a** $I_d - V_d$ curves of the hybrid graphene/Ti₂O₃ photodetector measured in dark and under quantum cascade laser illumination (λ : 10 μm ; power: 2 mW/cm^2); the gate voltage is 80 V. The channel size is 10.8 $\mu\text{m} \times 19.5 \mu\text{m}$. **b** Corresponding photocurrent of the hybrid graphene/Ti₂O₃ photodetector plotted as a function of bottom gate voltage. **c** Temporal response of the device to the illumination of 10 μm laser. **d** Responsivity of the hybrid graphene/Ti₂O₃ photodetector measured at different illumination wavelengths in the mid-infrared regime. The high responsivity measured in the wavelength regime from 4.5 to 10 μm demonstrated the broadband operation of the hybrid graphene/Ti₂O₃ photodetector. Error bars represent standard deviation. **e** Time-dependent photocurrent of the hybrid graphene/Ti₂O₃ photodetector with monolayer, bilayer and trilayer graphene. In the measurements of (c) and (e), the laser power was kept at 2 mW/cm^2 , and the source-drain voltage (V_d) and gate voltage (V_g) were kept at 2 mV and 80 V, respectively. **f** Noise spectra of monolayer, bilayer and trilayer graphene hybrid photodetectors as a function of frequency measured at a constant bias voltage of 5 mV. All the current noises show a typical trend of $S \sim 1/f^\alpha$ with $\alpha = 1$. **g** Photocurrents of hybrid graphene/Ti₂O₃ photodetectors with different sizes of Ti₂O₃ nanoparticles measured under 10 μm laser illumination. The measurement parameters are the same as in Fig. 4c, d. Error bars represent standard deviation. **h** Comparison of the performance of the hybrid graphene/Ti₂O₃ photodetector with the state-of-the-art

under the bias-optimized band alignment conditions. We also elucidate that the charge transfer efficiency increases with the number of graphene layers and achieves a high responsivity of $\sim 300 \text{ A W}^{-1}$ and detectivity of $\sim 7 \times 10^8 \text{ cm Hz}^{1/2} \text{ W}^{-1}$ at room temperature in the hybrid Ti₂O₃ device with trilayer graphene hybrid photodetectors. This work not only highlights the importance of exploring narrow-bandgap absorbers and tailoring the charge transfer process for hybrid graphene photodetectors

but also opens a venue for developing graphene-based optoelectronic devices for operation in the mid-infrared regime.

Methods

Fabrication of the Ti₂O₃ nanocrystals. Ti₂O₃ raw material was purchased from Sigma-Aldrich. Millipore filter membranes were purchased from Merck Millipore. Ti₂O₃ nanoparticles were obtained by using ball milling technique with Agate balls (diameter: 10 and 5 mm). Ethanol was added during milling, and the milling speed

was fixed at 300 rpm for 48 h. The size distribution of the obtained nanoparticles is shown in the Supplementary Figure 2. Different sizes of nanoparticles were achieved by tuning the centrifugation speed, as shown in the Supplementary Figure 3.

Light absorption measurements. The absorption spectra of the Ti_2O_3 nanoparticles spin-coated on KBr substrate were measured using a Fourier Transform Infrared Spectrometer (FTIR, VERTEX 70v). The measurements were all performed in the ambient conditions.

FET device fabrication. Graphene flakes were mechanically exfoliated from a crystal of highly oriented pyrolytic graphite (HOPG) using adhesive 3M-tape and deposited on a silicon wafer with a 285-nm thermalized SiO_2 layer. The location and quality of graphene were characterized by optical contrast using an optical microscope and Raman spectroscopy, respectively. Then, graphene-based FETs with the heavily doped silicon substrate as the backgate electrode were fabricated by standard photolithography and e-beam evaporation. Subsequently, the Ti_2O_3 nanoparticles were dispersed in ethanol solution (~5%, wt %) and spin-coated (4000 rpm) on the surface of the graphene channel. The devices were then dried in an oven under 100 °C for 12 h.

Electrical and optoelectronic measurements. The electrical characteristics were examined by a semiconductor parameter analyzer (Agilent, B1500A). The responsivity measurement was performed in a digital deep level transient spectroscopy (BIORAD) system with mid-infrared lasers (Tunable CW/Pulsed External Cavity Quantum Cascade Laser from 4.0 μm to 7 μm and 9.75 μm to 10.48 μm) to illuminate the whole devices, as shown in Supplementary Figure 4. The lasers beams are focused by IR lens with a spot size of ~100 μm , which is much larger than the active area of the devices. Noise spectra were acquired by a spectrum analyzer (Keysight M9018A). The measurement details are shown in Supplementary Note 2.

Data availability

The authors declare that the data supporting the findings of this study are available within the paper and its supplementary information files.

Received: 18 December 2017 Accepted: 17 September 2018

Published online: 16 October 2018

References

- Konstantatos, G. et al. Ultrasensitive solution-cast quantum dot photodetectors. *Nature* **442**, 180–183 (2006).
- Choe, J. W., o, B., Bandara, K. M. S. V. & Coon, D. D. Exchange interaction effects in quantum well infrared detectors and absorbers. *Appl. Phys. Lett.* **56**, 1679–1681 (1990).
- Palaferrri, D. et al. Room-temperature nine- μm -wavelength photodetectors and GHz-frequency heterodyne receivers. *Nature* **556**, 85–88 (2018).
- Lhuillier, E., Keuleyan, S., Zolotavin, P. & Guyot-Sionnest, P. Mid-infrared HgTe/As₂S₃ field effect transistors and photodetectors. *Adv. Mater.* **25**, 137–141 (2013).
- McDonald, S. A. et al. Solution-processed PbS quantum dot infrared photodetectors and photovoltaics. *Nat. Mater.* **4**, 138–142 (2005).
- Keuleyan, S., Lhuillier, E., Brajuskovic, V. & Guyot-Sionnest, P. Mid-infrared HgTe colloidal quantum dot photodetectors. *Nat. Photon* **5**, 489–493 (2011).
- Nikitskiy, I. et al. Integrating an electrically active colloidal quantum dot photodiode with a graphene phototransistor. *Nat. Commun.* **7**, 11954 (2016).
- Xia, F., Wang, H., Xiao, D., Dubey, M. & Ramasubramaniam, A. Two-dimensional material nanophotonics. *Nat. Photon* **8**, 899–907 (2014).
- Koppens, F. H. L. et al. Photodetectors based on graphene, other two-dimensional materials and hybrid systems. *Nat. Nanotechnol.* **9**, 780–793 (2014).
- De Sanctis, A. et al. Extraordinary linear dynamic range in laser-defined functionalized graphene photodetectors. *Sci. Adv.* **3**, e1602617 (2017).
- Xia, F., Mueller, T., Lin, Y.-m., Valdes-Garcia, A. & Avouris, P. Ultrafast graphene photodetector. *Nat. Nanotechnol.* **4**, 839–843 (2009).
- Wang, X. M., Cheng, Z. Z., Xu, K., Tsang, H. K. & Xu, J. B. High-responsivity graphene/silicon-heterostructure waveguide photodetectors. *Nat. Photon* **7**, 888–891 (2013).
- Freitag, M. et al. Photocurrent in graphene harnessed by tunable intrinsic plasmons. *Nat. Commun.* **4**, 1951 (2013).
- Furchi, M. et al. Microcavity-integrated graphene photodetector. *Nano Lett.* **12**, 2773–2777 (2012).
- García de Abajo, F. J. Graphene nanophotonics. *Science* **339**, 917–918 (2013).
- Sun, Z. et al. Infrared photodetectors based on CVD-grown graphene and PbS quantum dots with ultrahigh responsivity. *Adv. Mater.* **24**, 5878–5883 (2012).
- Konstantat, G. et al. Hybrid graphene-quantum dot phototransistors with ultrahigh gain. *Nat. Nanotechnol.* **7**, 363–368 (2012).
- Manga, K. K., Wang, S., Jaiswal, M., Bao, Q. & Loh, K. P. High-gain graphene-titanium oxide photoconductor made from inkjet printable ionic solution. *Adv. Mater.* **22**, 5265–5270 (2010).
- Guo, W. et al. Oxygen-assisted charge transfer between ZnO quantum dots and graphene. *Small* **9**, 3031–3036 (2013).
- Chen, S.-Y. et al. Biologically inspired graphene-chlorophyll phototransistors with high gain. *Carbon N. Y.* **63**, 23–29 (2013).
- Lee, Y. et al. High-performance perovskite-graphene hybrid photodetector. *Adv. Mater.* **27**, 41–46 (2014).
- Buscema, M., Groenendijk, D. J., Steele, G. A., van der Zant, H. S. J. & Castellanos-Gomez, A. Photovoltaic effect in few-layer black phosphorus PN junctions defined by local electrostatic gating. *Nat. Commun.* **5**, 4651 (2014).
- Yu, X., Zhang, S., Zeng, H. & Wang, Q. J. Lateral black phosphorene P–N junctions formed via chemical doping for high performance near-infrared photodetector. *Nano Energy* **25**, 34–41 (2016).
- Youngblood, N., Chen, C., Koester, S. J. & Li, M. Waveguide-integrated black phosphorus photodetector with high responsivity and low dark current. *Nat. Photon.* **9**, 247–252 (2015).
- Buscema, M. et al. Fast and broadband photoresponse of few-layer black phosphorus field-effect transistors. *Nano Lett.* **14**, 3347–3352 (2014).
- Yu, X. et al. Atomically thin noble metal dichalcogenide: a broadband mid-infrared semiconductor. *Nat. Commun.* **9**, 1545 (2018).
- Wang, J. et al. High-performance photothermal conversion of narrow-bandgap Ti_2O_3 nanoparticles. *Adv. Mater.* **29**, 1603730 (2017).
- Li, Y. et al. Orthorhombic Ti_2O_3 : a polymorph-dependent narrow-bandgap ferromagnetic oxide. *Adv. Funct. Mater.* **28**, 1705657 (2018).
- Mott, N. F. The basis of the electron theory of metals, with special reference to the transition metals. *Proc. Phys. Soc. A* **62**, 416 (1949).
- Cao, Y. et al. Correlated insulator behaviour at half-filling in magic-angle graphene superlattices. *Nature* **556**, 80–84 (2018).
- Chang, C. F. et al. c-Axis dimer and its electronic breakup: the insulator-to-metal transition in Ti_2O_3 . *Phys. Rev. X* **8**, 021004 (2018).
- Pan, S. S. et al. Self-doped rutile titania with high performance for direct and ultrafast assay of H_2O_2 . *ACS Appl. Mater. Interfaces* **5**, 12784–12788 (2013).
- Scanlon, D. O. et al. Band alignment of rutile and anatase TiO_2 . *Nat. Mater.* **12**, 798–801 (2013).
- Das, A. et al. Monitoring dopants by Raman scattering in an electrochemically top-gated graphene transistor. *Nat. Nanotechnol.* **3**, 210–215 (2008).
- Yu, X., Shen, Y., Liu, T., Wu, T. & Wang, Q. Photocurrent generation in lateral graphene p-n junction created by electron-beam irradiation. *Sci. Rep.* **5**, 12014 (2015).
- Yahia, J. & Frederikse, H. P. R. Electrical conduction in p-type titanium sesquioxide. *Phys. Rev.* **123**, 1257–1261 (1961).
- Yan, J., Zhang, Y., Kim, P. & Pinczuk, A. Electric field effect tuning of electron-phonon coupling in graphene. *Phys. Rev. Lett.* **98**, 166802 (2007).
- Pisana, S. et al. Breakdown of the adiabatic Born-Oppenheimer approximation in graphene. *Nat. Mater.* **6**, 198–201 (2007).
- Ferrari, A. C. & Basko, D. M. Raman spectroscopy as a versatile tool for studying the properties of graphene. *Nat. Nanotechnol.* **8**, 235–246 (2013).
- Gabor, N. M. et al. Hot carrier-assisted intrinsic photoresponse in graphene. *Science* **334**, 648–652 (2011).
- Yu, X., Dong, Z., Yang, J. K. W. & Wang, Q. J. Room-temperature mid-infrared photodetector in all-carbon graphene nanoribbon- C_{60} hybrid nanostructure. *Optica* **3**, 979–984 (2016).
- Yan, J. et al. Dual-gated bilayer graphene hot-electron bolometer. *Nat. Nanotechnol.* **7**, 472–478 (2012).
- Long, M. et al. Room temperature high-detectivity mid-infrared photodetectors based on black arsenic phosphorus. *Sci. Adv.* **3**, e1700589 (2017).
- Rogalski, A. Infrared detectors: an overview. *Infrared Phys. Technol.* **43**, 187–210 (2002).
- Haddadi, A., Chen, G., Chevallier, R., Hoang, A. M. & Razeghi, M. InAs/InAs_{1-x}Sb_x type-II superlattices for high performance long wavelength infrared detection. *Appl. Phys. Lett.* **105**, 121104 (2014).
- Rogalski, A. HgCdTe infrared detector material: history, status and outlook. *Rep. Prog. Phys.* **68**, 2267 (2005).
- Yu, X. et al. A high performance, visible to mid-infrared photodetector based on graphene nanoribbons passivated with HfO_2 . *Nanoscale* **8**, 327–332 (2016).
- Balandin, A. A. Low-frequency $1/f$ noise in graphene devices. *Nat. Nanotechnol.* **8**, 549–555 (2013).

Acknowledgements

This work is supported by funding from Ministry of Education, Singapore grant (MOE2016-T2-2-159, MOE2016-T2-1-128, MOE2015-T2-2-007, MOE Tier 1 RG164/15) and National Research Foundation, Competitive Research Program (NRF-CRP18-2017-02) and NSFC (61704082) and Natural Science Foundation of

Jiangsu Province (BK20170851). Y.L. and T.W. acknowledge funding support from the King Abdullah University of Science and Technology (KAUST).

Author contributions

X.Y., Q.W., Y.L. and T.W. conceived the project and designed the experiments. X.Y. and Y.L. performed material synthesis, device fabrication, characterization, data analysis and interpretation. D. Z., Y.T. and M.A H provided the TEM characterizations. X.H., Y.H. and Z.L. supported the device fabrications. Q.W. and T.W. supervised the project. All the authors contributed to the discussion of the manuscript. X.Y. and Y.L. contributed equally to this work.

Additional information

Supplementary Information accompanies this paper at <https://doi.org/10.1038/s41467-018-06776-z>.

Competing interests: The authors declare no competing interests.

Reprints and permission information is available online at <http://npg.nature.com/reprintsandpermissions/>

Publisher's note: Springer Nature remains neutral with regard to jurisdictional claims in published maps and institutional affiliations.



Open Access This article is licensed under a Creative Commons Attribution 4.0 International License, which permits use, sharing, adaptation, distribution and reproduction in any medium or format, as long as you give appropriate credit to the original author(s) and the source, provide a link to the Creative Commons license, and indicate if changes were made. The images or other third party material in this article are included in the article's Creative Commons license, unless indicated otherwise in a credit line to the material. If material is not included in the article's Creative Commons license and your intended use is not permitted by statutory regulation or exceeds the permitted use, you will need to obtain permission directly from the copyright holder. To view a copy of this license, visit <http://creativecommons.org/licenses/by/4.0/>.

© The Author(s) 2018